High-performance large-area blade-coated perovskite solar cells with low ohmic loss for low lighting indoor applications

Zhuoneng Bi,[1,2] Xueqing Xu,[1,2*] Xia Chen,[1] Yanqing Zhu,[1] Chang Liu, [3] Hua Yu, [3*] Yupeng Zheng,[1,2] Pavel A. Troshin,[4,5] Antonio Guerrero, [6] Gang Xu[1,2]

[1] Key Laboratory of Renewable Energy, Guangdong Key Laboratory of New and Renewable Energy Research and Development, Guangzhou Institute of Energy Conversion, Chinese Academy of Sciences, Guangzhou 510640, China

[2] Center of Materials Science and Optoelectronics Engineering, University of Chinese Academy of Sciences, Beijing 100049, China

[3] Institute of Photovoltaics, Southwest Petroleum University, Chengdu 610500, P. R. China

[4] Silesian University of Technology, Akademicka 2A, 44-100 Gliwice, Poland

[5] Institute for Problems of Chemical Physics of the Russian Academy of Sciences (IPCP RAS), Academician Semenov avenue 1, Chernogolovka, Moscow region, 142432 Russian Federation

[6] Institute of Advanced Materials (INAM), Universitat Jaume I, 12006 Castelló, Spain

[*] Corresponding author

email: xuxq@ms.giec.ac.cn, 17198328@qq.com

Abstract

Emerging hybrid organic-inorganic perovskites with superior optoelectronic property demonstrate promising prospect for photovoltaic applications, in particular for low-lighting indoor applications e.g. within internet of things (IoT) networks or low-energy wireless communication devices. In order to prepare devices with high power output under low-illumination conditions, scalable fabrication techniques are preferred

for large-area perovskite solar cells. In addition, one of the key parameters to achieve high-efficiency large-area perovskite solar cells is to minimize the ohmic loss to further boost the solar cell efficiency. Herein, a one-step blade-coating method assisted by hexafluorobenzene (HFB) was developed to deposit large-area smooth and defect-free perovskite films with low ohmic loss. The as-fabricated devices demonstrated power conversion efficiency (PCE) of 20.7% (area of 0.2 cm^2) and 16.5% (1 cm^2), respectively, under standard 1000 mW/cm^2 (AM1.5G) illumination conditions. Besides, the large-area (1 cm^2) devices demonstrated a remarkable PCE of ~32% under 0.1 mW/cm^2 (~285 lux) illumination provided by white light-emitting diode (LED) lamp for indoor lighting which strongly indicate that the fabricated large-area devices exhibited practical applications to be used in the vast majority of low-lighting indoor conditions ($\geqslant$100 lux). The analysis using a single diode model suggests that the high performance of the large-area devices under low-lighting indoor conditions is highly associated with the largely reduced ohmic losses of the perovskite films by a facile and scalable blade-coating method. The ohmic loss for the 1 cm^2 device was estimated as low as 1.66% at ~285 lux. The presented scalable approach paves the way to designing high-performance perovskite solar cells for a variety of emerging indoor PV applications.

Keywords: perovskite solar cells, blade-coating, large area, low-lighting indoor applications, ohmic loss

Introduction

Hybrid organic-inorganic perovskite solar cells (PSCs) have been demonstrated to be one of the most promising candidates for the next generation photovoltaics due to their high power conversion efficiency (PCE) and low materials and fabrication cost [1, 2]. PSCs have versatile promising applications in portable electronics, such as remote energy-independent sensors for the internet of things networks, or low-energy wireless communication devices [3-5]. Most of these devices need to work continuously under low

indoor illumination conditions (100 ~ 1000 lux) [5]. Low-lighting indoor photovoltaics has a very high demand in the current and future power-supply market [4]. Hence, the low-lighting indoor perovskite photovoltaics have recently emerged as one of the promising and practical technology for indoor power supply [6-11].

Organic-inorganic perovskite absorber materials is one of the ideal candidates for indoor photovoltaics since their absorption spectra perfectly match the emission spectra of LED or fluorescent lamps (400 - 800 nm) [12]. Recently, Liu et al. achieved an impressive PCE of 40.1% under indoor illumination conditions (824.5 lux) for the perovskite solar cell with a small active area of 0.08 cm^2 [12]. There are also multiple other reports on small-area PSCs delivering PCEs of 30 – 40% under indoor conditions. However, the small area device is not practically for commercialization use and the development of large-area indoor PSCs is impeded by large ohmic loss. Feng et al. have reported one of the highest records to date for large-area devices (2.25 cm^2) demonstrating excellent PCE of 30.6% under indoor condition (1000 lux)[13].

Generally, there are two popular approaches to improve PCE of PSCs under indoor illumination conditions. The first approach requires the devices achieving high shunt resistance (R_{sh}), which can effectively minimize ohmic losses under low-light conditions [14-16]. Interface modification is a common strategy to obtain high shunt resistance devices [6, 14]. The other approach is based on suppressing the charge carrier recombination losses, which is manifested in the diode ideality factors (n) close to 1 [10]. The ideality fact n can be estimated from the dependence of the open-circuit voltage (V_{OC}) on the incident light intensity [13]. Achieving good ideality factors requires suppressing trap-assisted recombination within the device. The passivation of traps and defects in the perovskite films is an effective way to reduce V_{OC} losses [12].

For potential practical applications, low-lighting perovskite solar cells should be produced using scalable techniques compatible with the roll-to-roll process. However, most of the perovskite films reported so far prepared by non-scalable methods such as spin-coating. To date, large-area deposition methods remain insufficiently investigated. The first reports on blade-coating were published in 2015, and presented PSCs with the PCEs of 11-15% produced using DMF as a solvent [17, 18]. More recently, meniscus-

assisted technique produced large-grain perovskite films, which boosted the device efficiency up to 20% (using DMSO as a solvent) [19]. Solvent mixtures of DMSO and gamma-butyrolactone (GBL) were previously used to fabricate PSCs with the PCE of about 18% [20, 21]. Further development of the blade-coating techniques for PSCs fabrication is commonly considered as one of the most promising steps towards large-scale commercial applications of PSCs [2, 22-25].

In this work, we present a one-step blade-coating assisted by HFB approach to deposit high-quality defect-free perovskite films for indoor perovskite photovoltaics. The proposed method produces highly crystalline perovskite films in a single step by using engineered inks based on a low inhalation toxic solvent mixture of DMSO, GBL and HFB. The preheating of the precursor ink enables complete dissolution of PbI_2 and MAI in the mixed solvent close to the solubility limit. It is found that the HFB additive effectively smooths down the perovskite films and passivate the defects, thus, the as-fabricated devices demonstrate high power conversion efficiency (PCE) of 20.7% on a small area of 0.2 cm^2 and 16.5% on the area of 1 cm^2 under standard 1 sun (AM1.5G) illumination conditions. Furthermore, the large-area (1 cm^2) devices deliver a remarkable PCE of ~32% under 0.1 mW/cm^2 (~285 lux) illumination provided by light-emitting diode (LED) lamp.

Results and discussion

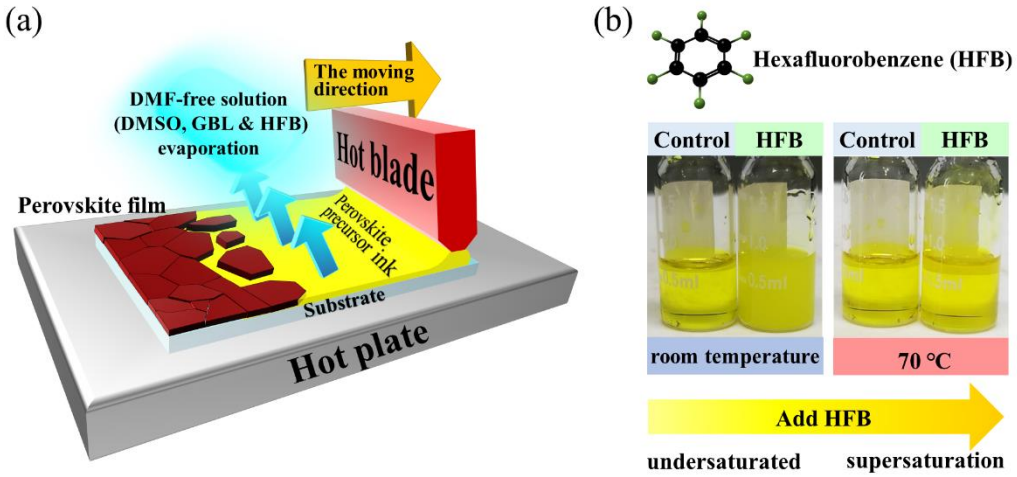

Figure 1. a) Schematic diagram of the HFB-assisted one-step blade-coating method to

produce high-quality defect-free $MAPbI_3$ film. b) Photographs of $MAPbI_3$ precursor solutions with and without HFB at room temperature and at 70 °C.

Figure 1a shows the schematic diagram of the blade-coating setup to produce $MAPbI_3$ perovskite films. In the experimental process the substrate is fixed on a hotplate with a blade set above the substrate forming the slit of around 100 µm. The perovskite precursor ink is injected into the slit and the pre-heating blade immediately moves horizontally on the heating substrate. With the solvent evaporating, the black perovskite film forms in a couple of seconds. The one-step blade coating process is very simple and adapts to different process variations. In addition, for further improve the quality of perovskite films on this one-step blade coating approach the solvent may be easily modified. In particular we observe that the use of a co-solvent HFB in the perovskite precursor is beneficial for the film quality. Further details of the one-step blade-coating process are given in the experimental section.

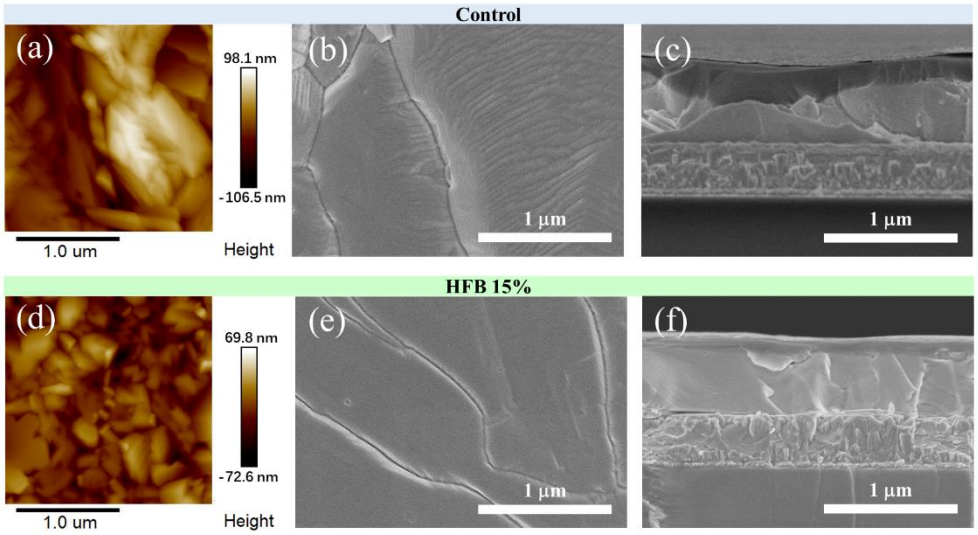

Figure 2. a, d) AFM images of the Control and HFB 15% $MAPbI_3$ films. b, e) Top-view and c, f) cross-section SEM images of the Control HFB 15% samples.

Figure 1b shows a image of the reference precursor solution and the modified ink loaded with HFB additive. HFB is a low inhalation toxic organic solvent that is commonly used in medicine [26]. HFB is immiscible with water, but it can be miscible with DMSO in a certain proportion [27]. At room temperature, perovskite inks with HFB additive are non-transparent, which indicates incomplete material solubilization but to the presence of a bad solvent (or anti-solvent) such as HFB. However, preheating the

precursor solution at 70 ºC results in complete solubilization of PbI_2 and MAI and formation of transparent solution with material concentrations close to the solubility limit leading to saturated solutions.

Figure S1 shows the scanning electron microscopy (SEM) images of the $MAPbI_3$ films prepared from the inks with different HFB loadings and marked as Control (corresponds to HFB 0%), HFB 5%, HFB 10%, and HFB 15%. All samples exhibit spherulitic growth and large gain size with no voids or pinholes. The Control and HFB 15% samples display obvious difference between as illustrated by the SEM images shown in Figures 2b and 2e. The HFB 15% sample exhibits a flat and uniform crystalline grain surface, whereas the Control sample has wavy surface morphology. The surface topography of the films was further studied by atomic force microscopy (AFM) as shown in Figure 2a and 2d. The root-mean-square roughness values for the Control and HFB 15% samples were determined as 28.1 and 20.5 nm, respectively, which is consistent with the SEM images. The cross-section SEM images (Figures 2c, 2f and S2) reveal the average thickness of perovskite films as ~415 nm and ~438 nm for Control and HFB 15% samples, respectively. It is worth noting that the HFB 15% sample shows a more uniform structure and thickness of the perovskite film.

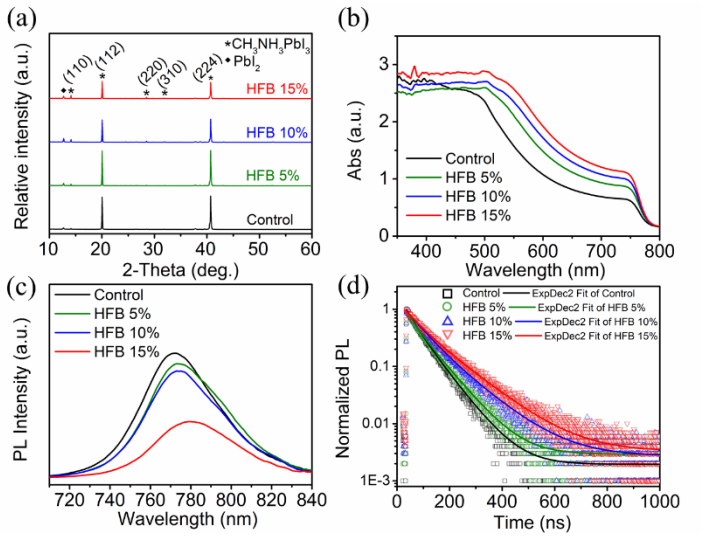

Figure 3. Characterization of the $MAPbI_3$ films with different HFB loadings on the glass/FTO/SnO_2-PbO/SnO_2 substrates. a) XRD diffraction patterns. b) UV-vis absorption spectra. c) Steady-state PL spectra. d) Time-resolved PL (TRPL) profiles.

The effect of the HFB additive on the structural and optical properties of perovskite films is illustrated in Figure 3a and Figure 3b, respectively. All samples show similar peaks on the x-ray diffraction (XRD) patterns, indicating a high phase purity of the perovskites. The diffraction peaks at 14.12˚ 20.02˚ 28.46˚ 31.90˚ and 40.70˚ can be assigned to (110), (112), (220), (310), and (224) crystal planes of the tetragonal $MAPbI_3$ perovskite lattice, respectively [18]. The sharp and intense (112) diffraction peaks indicate a highly oriented crystal structure of the films. Interestingly, the addition of HFB increases the intensity of (110) peaks, suggesting improved film crystallization.

The absorption spectra become significantly stronger with increasing the HFB loading from 0% to 15%. We believe that the uniform thickness of HFB-processed films helps to avoid absorption losses, while in the case of Control samples some light passes through the voids or deep valleys in the films. Thus, the obtained results reveal that HFB can not only make the perovskite films more uniform but also alter the crystal growth and enhance film absorbance.

Figures 3c and 3d show steady-state photoluminescence (PL) and time-resolved photoluminescence (TRPL) spectra. The PL peaks of the HFB processed sample are red-shifted compared to that of the Control sample and the magnitude of the red-shift is proportional to the HFB loading with a ~7 nm peak shift for the HFB 15% sample. Furthermore, a red-shift of the low-energy absorption onset was observed, which in combination with PL data implies that the HFB-processed samples have a slightly lower bandgap as compared to the Control, which could be a consequence of the enhanced material crystallinity. The charge carrier lifetimes in the HFB-processed samples were considerably longer than that of the Control (τ_1= 36.0 ns and τ_2= 73.7 ns) sample and the lifetime increase was proportional with the HFB loading. In particular, the HFB 15% sample showed almost twice longer lifetimes (τ_1 = 52.7 ns and τ_2= 122.8 ns) as compared to the Control sample, which evidences that HFB additive effectively suppresses trap-assisted carrier recombination due to the formation of high-quality perovskite grains with a low density of defects.

Fabrication and characterization of photovoltaic devices

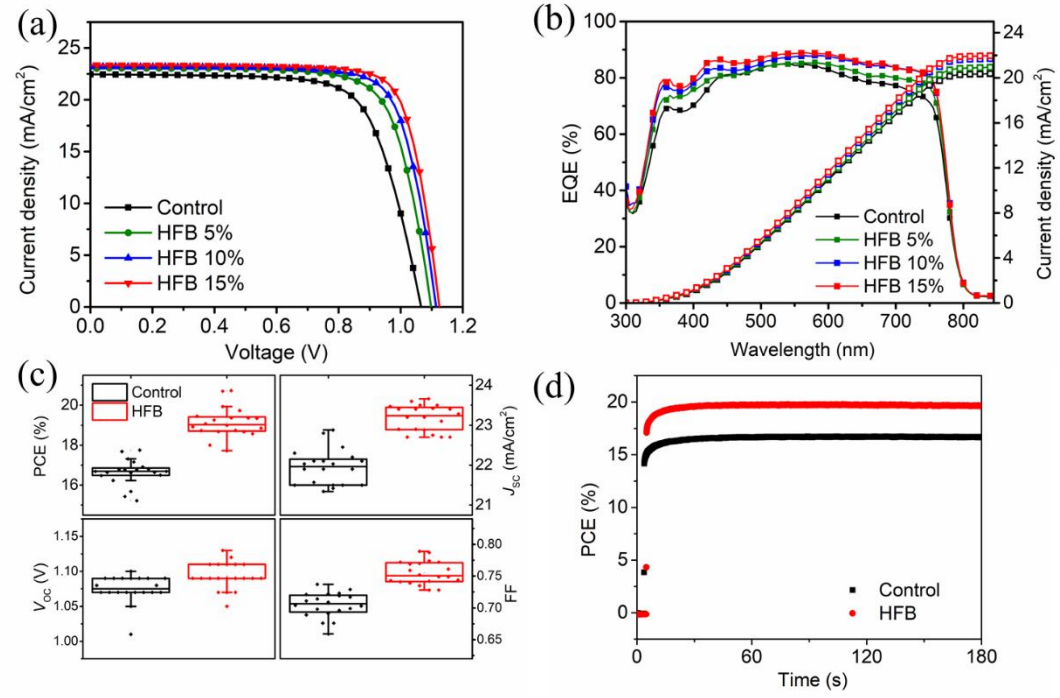

Figure 4. a) *J-V* curves measured under standard 100 mW cm^{-2} AM1.5G simulated illumination conditions. b) EQE spectra of the devices. c) Statistics for 20 Control and 20 HFB 15% devices. d) Stabilized output measurements in the maximum power point tracking regime under the standard illumination conditions.

Photovoltaic devices were fabricated with device architecture of Glass/FTO/SnO_2-PbO/SnO_2/$MAPbI_3$/Spiro-OMeTAD/Au. The $MAPbI_3$ films were prepared with different HFB loadings in the precursor ink, which are marked as Control, HFB 5%, HFB 10%, and HFB 15% samples. Further details on the device fabrication can be found in the Experimental section. It is worth mentioning that the deposition of $MAPbI_3$ by the developed one-step blade coating method does not require any additional steps such as solvent annealing or anti-solvent bath, etc. The representative *J-V* curves measured under the simulated 1 sun illumination conditions are presented in Figure 4a, whereas the corresponding device parameters are summarized in Table S1.

The Control devices show PCE exceeding 17%, which is in good agreement with the previously reported characteristics of the $MAPbI_3$ devices fabricated in dry box conditions with a relative humidity between 10% to 20%. However, increasing of HFB amount in the ink improves the photovoltaic performance of the devices processed under the same conditions. Using the optimal amount of HFB (15%), the champion

cells with a PCE of 20.7%, open-circuit voltage V_{OC} of 1.13 V, short-circuit current density J_{SC} of 23.4 mA/cm^2, and fill factor FF of 78.4% was achieved. The stabilized output measurements of the PCE and photocurrent density of the champion cell delivered the values of 19.8% and 21.9 mA/cm^2, respectively (Figure 4d). The obtained photocurrent density is in good agreement with the integrated J_{SC} extracted from the EQE spectrum by its integration over the reference solar AM1.5G spectrum (Figure 4b). The statistics for 20 devices of each type (Figure 4c) show a remarkable improvement in average PCE from 16.6% to 19.1% when HFB is incorporated into the precursor inks. Furthermore, it was surprising that HFB additive also improves the environmental stability of the devices as shown in Figure S4. Thus, HFB could be considered as a highly promising co-solvent for perovskite inks and processing additive improving simultaneously the efficiency and stability of PSCs.

Design and characterization of large-area PSCs for low lighting indoor applications

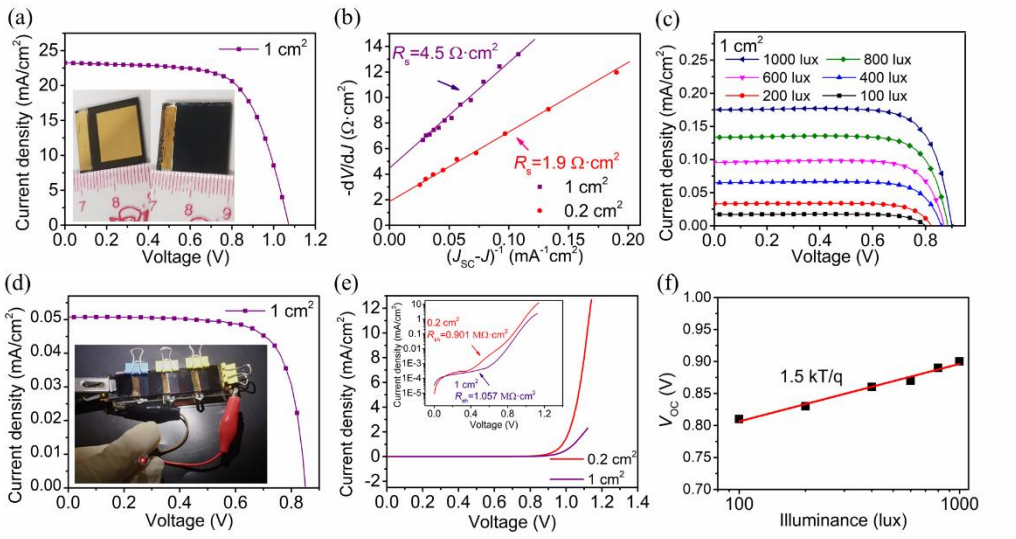

Figure 5. a) *J-V* curve of the fabricated device with an active area of 1 cm^2 measured under simulated 1 sun illumination conditions. b) The linear dependences of -d*V*/d*J vs.* $(J_{SC}\text{-}J)^{-1}$ for devices with different active area sizes c) *J-V* curves of 1 cm^2 cell measured under different illumination intensities provided by white-light LED. C) *J-V* curve under 0.1 mW/cm^2 (~285 lux) white LED. e) *J-V* curves measured in the dark for devices with different active area sizes; insert shows the estimation of R_{sh} values. f) V_{OC} plot as a function of illuminance for the calculation of ideality factor.

The results above demonstrated that the one-step blade-coating method assisted by HFB could produces smooth and defect-free perovskite films, which enable the fabrication of large-area photovoltaic devices. The optimal addition amount of HFB is 15%, based on this, we prepared large-area devices and studied their practical application performance in indoor low-lighting conductions (Figure 5). A modest reduction in PCE from 20.7% to 16.5% was observed when the device area was increased from 0.2 cm^2 to 1 cm^2 (Figure 5a). The main reason for the PCE reduction was the increase in the length of the electrodes with a limited conductivity (particularly FTO), which leads to the increased series resistance (R_s) [2, 28]. R_s can be estimated from *J-V* curves as shown in Figure 5b, the detailed calculation method can be found in the literature [29]. The R_s values of the 0.2 cm^2 and the 1 cm^2 devices were 1.9 $\Omega \cdot cm^2$ and 4.5 $\Omega \cdot cm^2$, respectively.

The low-lightning indoor photovoltaic test carried out under a white LED light. The *J-V* curve of the 1 cm^2 device measured with the intensity of 0.1 mW/cm^2 (~285 lux) is displayed in Figure 5d. The 1 cm^2 device exhibited a remarkable PCE of 31.7% (J_{SC}=0.0506 mA/cm^2, V_{OC}=0.85 V, FF=74%). Figure 5d shows the series-connected stack of large-area perovskite solar cells powering up a red LED under indoor illumination conditions. Furthermore, the solar cells can operate efficiently at ~260 lux of the fluorescent lamp light (common indoor conditions) as shown in Figure S6.

The *J-V* characteristics measured under different illumination (100 to 1000 lux) conditions using white-light LED are shown in Figure 5c. The PCEs of 33.8% and 30.0% were achieved at 1000 lux and 100 lux, respectively. It is worth mentioning that the fabricated devices can be used in almost any indoor light environment. The diode ideality factor for the 1 cm^2 device was estimated to be 1.5 as shown in Figure 5f.

High shunt resistance can effectively suppress shunting losses in the devices under low-light conditions. The shunt resistance can be estimated from the dark *J-V* curves as shown in Figure 5d, whereas the detailed calculation method can be found literature [14, 30]. The R_{sh} values of 0.2 cm^2 and 1 cm^2 devices were found to be ~0.90 and ~1.06 M $\Omega \cdot cm^2$, respectively. Both values are quite high, so we consider that if each of the

device's functional layers is uniform and defect-free, the R_{sh} becomes independent of the device's active area. Besides, The R_{sh} values of 1 cm^2 Control device were found to be ~49.4 K$\Omega \cdot cm^2$, and it was shown that the R_{sh} of HFB 15% device is about 20 times higher than that of Control device, their dark *J-V* curves as shown in Figure S5. The analysis of the power losses caused by R_s and R_{sh} under different light intensities was using the single diode model presented in the next section.

Understanding of Ohmic losses of solar cells under different light intensity from single diode model

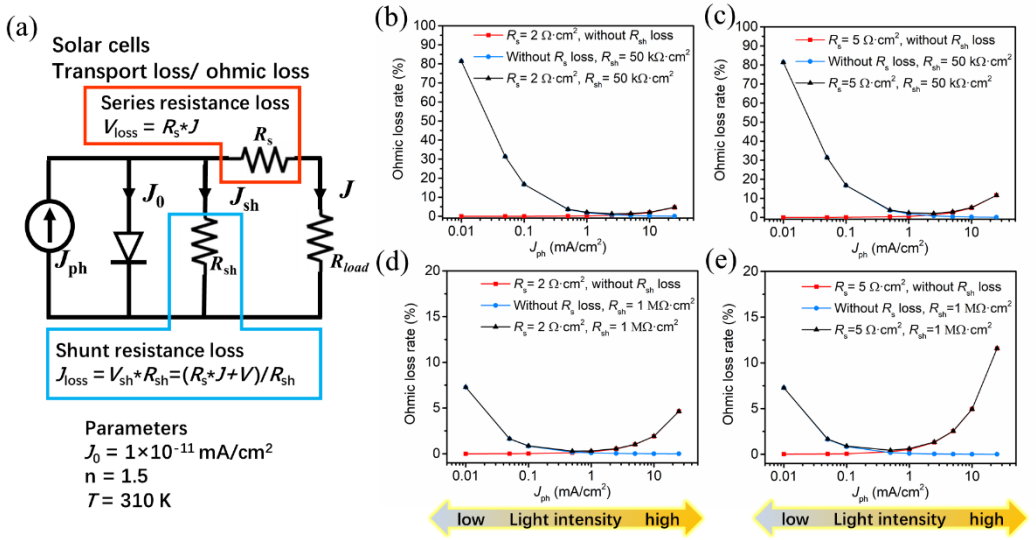

Figure 6. a) Equivalent circuit of solar cell. b) Simulated ohmic loss rate-J_{ph} curves for low R_{sh} (50 k$\Omega \cdot cm^2$) and low R_s (2 $\Omega \cdot cm^2$) device. c) Simulated ohmic loss rate-J_{ph} curves for low R_{sh} (50 k$\Omega \cdot cm^2$) and high R_s (5 $\Omega \cdot cm^2$) device. d) Simulated ohmic loss rate-J_{ph} curves for high R_{sh} (1 M$\Omega \cdot cm^2$) and low R_s (2 $\Omega \cdot cm^2$) device. e) Simulated ohmic loss rate-J_{ph} curves for high R_{sh} (1 M$\Omega \cdot cm^2$) and high R_s (5 $\Omega \cdot cm^2$) device.

There are three major types of power losses in solar cells, namely optical loss, nonradiative recombination loss and ohmic loss [31]. Here, the single diode model is used to analyze ohmic loss, and the schematic with the solar cell equivalent circuit is shown in Figure 6a. Ohmic loss is composed of series resistance loss and shunt resistance loss. The series resistance causes the loss of output voltage $V_{loss} = R_s j$. The shunt resistance causes the loss of output current ($J_{loss} = V_{sh}*R_{sh} = (R_s*J+V)/R_{sh}$). Obviously, Ohmic loss is a function of J_{ph}, in other words, the ohmic loss is a function of the light

intensity. The complete formula of single diode model can find in the support information. According to the single diode model [14, 32], we simulate the Ohmic loss rate-J_{ph} relationship curves as shown in Figures 6b to 6e. Here, Ohmic loss rate is defined as $(P_{m,\,ideal} - P_{m,\,ohmic})/P_{m,\,ideal}$, $P_{m,\,ideal}$ is the maximum output power without ohmic loss, $P_{m,\,ohmic}$ is the maximum output power with ohmic loss. The red lines represent the series loss rate, which decreases as the J_{ph} decreases. The blue lines represent the shunt loss rate, which increases as the J_{ph} decreases. The black lines represent the total ohmic loss. As follows from the comparison of Figures 6c and 6e, high shunt resistance can effectively minimize the ohmic loss under low light conditions. If we consider the actual values of parameters calculated from the devices in this work, the 1 cm^2 HFB-processed device would correspond to Figure 6e, so the ohmic loss rate would be only about 1.66% at 0.1 mW/cm^2 (~285 lux) under a white-light LED illumination. In addition, we found an interesting result. When under indoor low light conditions, ohmic loss mainly cause from shunt loss; when under outdoor conditions (near 1 sun condition) ohmic loss mainly cause from series loss. Therefore, optimizing R_{sh} is more important than optimizing R_s for indoor photovoltaics devices. These calculations match well with the experimental data, Thus, it can be concluded that the well-designed salable blade-coating method provides practical solutions for fabricated large-area perovskite films with low ohmic loss for high PCE perovskite solar cells under low-lighting indoor conditions.

Conclusions

To summarize, we have developed an efficient one-step blade-coating method to deposit large-area smooth and uniform perovskite films. The key approach is based on using hexafluorobenzene HFB as a co-solvent as well as processing additive, which improves film crystallinity, enhances absorbance and eliminates structural defects and traps. Furthermore, HFB allows performing the solar cell fabrication under ambient conditions in the air with controlled humidity and achieving impressive device power conversion efficiencies going beyond 20% for small-area cells. Owing to the fact that the developed HFB-assisted blade-coating method produces highly uniform and defect-free films, we succeeded in the fabrication of large-area devices and demonstration of

their high performance under indoor illumination conditions. In particular, the 1 cm^2 cell showed the PCE of 16.5% under simulated 1 sun AM1.5G illumination conditions and ~32% under the 0.1 mW/cm^2 (~285 lux) indoor illumination provided by white LED. We provide a method for estimating ohmic losses and calculate the ohmic loss rate of the 1 cm^2 device is 1.66% at ~285 lux. A comprehensive analysis revealed that the high efficiency of the fabricated large-area devices is enabled by the reduced ohmic losses under low light intensities.

Experimental section

Materials

PbI_2, CH_3NH_3I (MAI) and Spiro-OMeTAD were purchased from Xi'an Polymer Light Technology Corp. 4-tert-butylpyridine (TBP) was purchased from TCI. The SnO_2 solution (tin (IV) oxide, 15 wt% in H_2O colloidal dispersion) was obtained from Alfa Aesar. DMSO and lithium bis(trifluoromethanesulfonyl) imide (Li-TFSI) (99.95%) were purchased from Sigma-Aldrich Inc. Hexafluorobenzene (HFB) (98%) was purchased from Macklin. Other materials were purchased from Aladdin.

The perovskite precursor solutions

The perovskite precursor solution (Control) was prepared by dissolving MAI and PbI_2 in 1: 1.01 molar ratio in a mixture of GBL and DMSO. The GBL: DMSO ratio was varied during the optimization. The best results were obtained using 1.7 M concentration of the perovskite precursor and 14 : 11 v/v ratio of GBL to DMSO, which corresponds to 395.7 mg of PbI_2, 135.2 mg of MAI, 280 μL of GBL, and 220 μL of DMSO. The perovskite precursor solutions loaded with HFB were prepared simply by adding the appropriate volume of HFB (5%, 10% or 15%) to the perovskite precursor solution prepared as described above. The HFB-loaded solutions were heated at 70 °C on a hotplate until used.

Device fabrication

FTO-coated glass substrates (14 Ω/□) were patterned by etching with zinc powder and HCl (2 M). The etched substrates were ultrasonically cleaned with a soap solution, deionized water, ethanol, and isopropanol, respectively, and then dried under a stream of nitrogen. The preparation of the SnO_2-PbO composite electron transport layer (ETL) was performed following a previously reported procedure [14]. The coated ETL films were treated in a UV–O_3 cleaner for 15 min. The blade-coating of the perovskite films was performed in a dry box (R.H. 10% ~ 20%). The perovskite precursor solution (20 μL) was coated using a doctor blade coater (Zehntner ZAA 2300) at the substrate temperature of 150 °C. The gap between the blade and the substrate was 100 μm and the blade speed was 10 mm/s. The perovskite dark phase was formed within the first few seconds. The hole-transport material (HTM) solution was prepared by mixing 72.3 mg of spiro-OMeTAD, 28.8 μLof TBP, and 17.5 μL of LiTFSI solution (520 mg of LiTFSI in 1 ml of acetonitrile) in 1 ml of chlorobenzene. The HTM solution was spin-coated onto the perovskite films at 4000 rpm for 30 s. Finally, 50 nm thick gold electrodes were thermally evaporated on top of the doped spiro-OMeTAD HTM film to complete the device structure.

Film and Device Characterization

Morphology and microstructural characterization were performed using a SU-70 high-resolution analytical scanning electron microscope (SEM) (Hitachi, Japan). The X-ray diffraction (XRD) measurements were carried out on X'Pert PRO MPD X-ray diffractometer using Cu Kα irradiation at a scan rate (2θ) of 0.0167 deg. s^{-1}. UV-vis absorption spectra were measured using Perkin Elmer Lambda 750 UV/VIS/NIR spectrophotometer. The PL spectra and lifetime measurements for the perovskite films were conducted using an Edinburg fluorescence spectrometer (FLS980). The current density-voltage (*J-V*) curves were measured using an Autolab TYPE II electrochemical work station. A Keithley 2420 source meter at 100 mA/cm^2 AM1.5G illumination provided by the ABET Sun 3000 solar simulator. The light intensity was adjusted with an NREL-calibrated silicon solar cell. The white light LED and indoor condition light intensity were measured using TENMARS TM-208. The solar cells were masked with

an aperture to define the active area of 0.2 cm^2 or 1 cm^2. EQE measurements were carried out using an EQE system from Enli Technology Co., Ltd. All the characterization of the solar cells was performed under an ambient atmosphere at room temperature without any encapsulation.

Acknowledgments

This work is supported by the Project on Collaborative Innovation and Environmental Construction Platform of Guangdong Province (No. 2018A050506067). We also thank the financial support from the Key Laboratory of Renewable Energy, Chinese Academy of Sciences (y807j71001), Guangdong Provincial Key Laboratory of New and Renewable Energy Research and Development (Grant No. 2021E139kf0101), Key Project on Synergy Collaborative Innovation of Guangzhou City (201704030069), University Jaume I is also acknowledged for financial support (UJI-B2020-49), and the PAT acknowledges the support from the Russian Science Foundation (project No. 18-13-00205-P).

References

1. Kaltenbrunner, M.; Adam, G.; Glowacki, E. D.; Drack, M.; Schwodiauer, R.; Leonat, L.; Apaydin, D. H.; Groiss, H.; Scharber, M. C.; White, M. S.; Sariciftci, N. S.; Bauer, S., Flexible high power-per-weight perovskite solar cells with chromium oxide-metal contacts for improved stability in air. *Nat Mater* **2015,** *14* (10), 1032-+.

2. Cheng, Y. H.; Peng, Y.; Jen, A. K. Y.; Yip, H. L., Development and Challenges of Metal Halide Perovskite Solar Modules. *Sol Rrl* **2021**.

3. Hu, X. T.; Li, F. Y.; Song, Y. L., Wearable Power Source: A Newfangled Feasibility for Perovskite Photovoltaics. *Acs Energy Lett* **2019,** *4* (5), 1065-1072.

4. Mathews, I.; Kantareddy, S. N.; Buonassisi, T.; Peters, I. M., Technology and Market Perspective for Indoor Photovoltaic Cells. *Joule* **2019,** *3* (6), 1415-1426.

5. Polyzoidis, C.; Rogdakis, K.; Kymakis, E., Indoor Perovskite Photovoltaics for the Internet of Things-Challenges and Opportunities toward Market Uptake. *Adv Energy Mater* **2021,** *11* (38).

6. Dagar, J.; Castro-Hermosa, S.; Lucarelli, G.; Cacialli, F.; Brown, T. M., Highly efficient perovskite solar cells for light harvesting under indoor illumination via solution processed SnO2/MgO composite electron transport layers. *Nano Energy* **2018,** *49*, 290-299.

7. Chen, C. Y.; Chang, J. H.; Chiang, K. M.; Lin, H. L.; Hsiao, S. Y.; Lin, H. W., Perovskite Photovoltaics for Dim-Light Applications. *Adv Funct Mater* **2015,** *25* (45), 7064-7070.

8. Lucarelli, G.; Di Giacomo, F.; Zardetto, V.; Creatore, M.; Brown, T. M., Efficient light harvesting from flexible perovskite solar cells under indoor white light-emitting diode illumination. *Nano Res* **2017,** *10* (6), 2130-2145.

9. Di Giacomo, F.; Zardetto, V.; Lucarelli, G.; Cina, L.; Di Carlo, A.; Creatore, M.; Brown, T. M., Mesoporous perovskite solar cells and the role of nanoscale compact layers for remarkable all-round high efficiency under both indoor and outdoor illumination. *Nano Energy* **2016,** *30*, 460-469.

10. Ann, M. H.; Kim, J.; Kim, M.; Alosaimi, G.; Kim, D.; Ha, N. Y.; Seidel, J.; Park, N.; Yun, J. S.; Kim, J. H., Device design rules and operation principles of high-power perovskite solar cells for indoor applications. *Nano Energy* **2020,** *68*.

11. Wang, K. L.; Zhou, Y. H.; Lou, Y. H.; Wang, Z. K., Perovskite indoor photovoltaics: opportunity and challenges. *Chem Sci* **2021,** *12* (36), 11936-11954.

12. He, X. L.; Chen, J. Z.; Ren, X. D.; Zhang, L.; Liu, Y. C.; Feng, J. S.; Fang, J. J.; Zhao, K.; Liu, S. Z., 40.1% Record Low-Light Solar-Cell Efficiency by Holistic Trap-Passivation using Micrometer-Thick Perovskite Film. *Adv Mater* **2021,** *33* (27).

13. Cheng, R.; Chung, C. C.; Zhang, H.; Liu, F. Z.; Wang, W. T.; Zhou, Z. W.; Wang, S. J.; Djurisic, A. B.; Feng, S. P., Tailoring Triple-Anion Perovskite Material for Indoor Light Harvesting with Restrained Halide Segregation and Record High Efficiency Beyond 36%. *Adv Energy Mater* **2019,** *9* (38).

14. Bi, Z. N.; Zhang, S. H.; Thandapani, M.; Zhu, Y. Q.; Zheng, Y. P.; Liem, N. Q.; Xiao, X. D.; Xu, G.; Guerrero, A.; Xu, X. Q., High Shunt Resistance SnO2-PbO Electron Transport Layer for Perovskite Solar Cells Used in Low Lighting Applications. *Adv Sustain Syst* **2021**.

15. Proctor, C. M.; Nguyen, T. Q., Effect of leakage current and shunt resistance on the light intensity dependence of organic solar cells. *Appl Phys Lett* **2015,** *106* (8).

16. Steim, R.; Ameri, T.; Schilinsky, P.; Waldauf, C.; Dennler, G.; Scharber, M.; Brabec, C. J., Organic photovoltaics for low light applications. *Sol Energ Mat Sol C* **2011,** *95* (12), 3256-3261.

17. Yang, Z. B.; Chueh, C. C.; Zuo, F.; Kim, J. H.; Liang, P. W.; Jen, A. K. Y., High-Performance Fully Printable Perovskite Solar Cells via Blade-Coating Technique under the Ambient Condition. *Adv Energy Mater* **2015,** *5* (13).

18. Deng, Y. H.; Peng, E.; Shao, Y. C.; Xiao, Z. G.; Dong, Q. F.; Huang, J. S., Scalable fabrication of efficient organolead trihalide perovskite solar cells with doctor-bladed active layers. *Energ Environ Sci* **2015,** *8* (5), 1544-1550.

19. He, M.; Li, B.; Cui, X.; Jiang, B. B.; He, Y. J.; Chen, Y. H.; O'Neil, D.; Szymanski, P.; El-Sayed, M. A.; Huang, J. S.; Lin, Z. Q., Meniscus-assisted solution printing of large-grained perovskite films for high-efficiency solar cells. *Nat Commun* **2017,** *8*.

20. Bi, Z. N.; Rodriguez-Martinez, X.; Aranda, C.; Pascual-San-Jose, E.; Goni, A. R.; Campoy-Quiles, M.; Xu, X. Q.; Guerrero, A., Defect tolerant perovskite solar cells from blade coated non-toxic solvents. *J Mater Chem A* **2018,** *6* (39), 19085-19093.

21. Li, J. B.; Munir, R.; Fan, Y. Y.; Niu, T. Q.; Liu, Y. C.; Zhong, Y. F.; Yang, Z.; Tian, Y. S.; Liu, B.; Sun, J.; Smilgies, D. M.; Thoroddsen, S.; Amassian, A.; Zhao, K.; Liu, S. Z., Phase Transition Control for High-Performance Blade-Coated Perovskite Solar Cells. *Joule* **2018,** *2* (7), 1313-1330.

22. Liu, K.; Liang, Q.; Qin, M. C.; Shen, D.; Yin, H.; Ren, Z. W.; Zhang, Y. K.; Zhang, H. K.; Fong, P. W. K.; Wu, Z. H.; Huang, J. M.; Hao, J. H.; Zheng, Z. J.; So, S. K.; Lee, C. S.; Lu, X. H.; Li, G., Zwitterionic-Surfactant-Assisted Room-Temperature Coating of Efficient Perovskite Solar Cells. *Joule* **2020,** *4* (11), 2404-2425.

23. Deng, Y. H.; Zheng, X. P.; Bai, Y.; Wang, Q.; Zhao, J. J.; Huang, J. S., Surfactant-controlled ink drying enables high-speed deposition of perovskite films for efficient photovoltaic modules. *Nat Energy* **2018,** *3* (7), 560-566.

24. Cheng, J.; Liu, F.; Tang, Z. Q.; Li, Y. L., Scalable Blade Coating: A Technique Accelerating the Commercialization of Perovskite-Based Photovoltaics. *Energy Technol-Ger* **2021,** *9* (8).

25. Huang, F.; Li, M. J.; Siffalovic, P.; Cao, G. Z.; Tian, J. J., From scalable solution fabrication of perovskite films towards commercialization of solar cells. *Energ Environ Sci* **2019,** *12* (2), 518-549.

26. Antognini, J. F.; Raines, D. E.; Solt, K.; Barter, L. S.; Atherley, R. J.; Bravo, E.; Laster, M. J.; Jankowska, K.; Eger, E. I., 2nd, Hexafluorobenzene acts in the spinal cord, whereas o-difluorobenzene acts in both brain and spinal cord, to produce immobility. *Anesth Analg* **2007,** *104* (4), 822-8.

27. Zhuchkov, V. I.; Frolkova, A. K.; Nazanskiy, S. L., Experimental research and mathematical modeling of vapor-liquid equilibrium in the ternary benzene-hexafluorobenzene-dimethyl sulfoxide system. *Russ Chem B+* **2018,** *67* (2), 200-205.

28. Li, D. Y.; Jiang, P.; Zhang, W. H.; Du, J. K.; Qiu, C.; Liu, J. L.; Hu, Y.; Rong, Y. G.; Mei, A. Y.; Han, H. W., Series Resistance Modulation for Large-Area Fully Printable Mesoscopic Perovskite Solar Cells. *Sol Rrl* **2021**.

29. Bi, Z. N.; Liang, Z. R.; Xu, X. Q.; Chai, Z. S.; Jin, H.; Xu, D. H.; Li, J. L.; Li, M. H.; Xu, G., Fast preparation of uniform large grain size perovskite thin film in air condition via spray deposition method for high efficient planar solar cells. *Sol Energ Mat Sol C* **2017,** *162*, 13-20.

30. Barbato, M.; Meneghini, M.; Cester, A.; Mura, G.; Zanoni, E.; Meneghesso, G., Influence of Shunt Resistance on the Performance of an Illuminated String of Solar Cells: Theory, Simulation, and Experimental Analysis. *Ieee T Device Mat Re* **2014,** *14* (4), 942-950.

31. Sha, W. E. I.; Zhang, H.; Wang, Z. S.; Zhu, H. L.; Ren, X. G.; Lin, F.; Jen, A. K. Y.; Choy, W. C. H., Quantifying Efficiency Loss of Perovskite Solar Cells by a Modified Detailed Balance Model. *Adv Energy Mater* **2018,** *8* (8).

32. Jain, A.; Kapoor, A., Exact analytical solutions of the parameters of real solar cells using Lambert W-function. *Sol Energ Mat Sol C* **2004,** *81* (2), 269-277.